Deformation, Residual Stress, and Constitutive Relations for Quenched W319 Aluminum

M.L. NEWMAN, B.J. ROBINSON, H. SEHITOGLU, and J.A. DANTZIG

A study of the development of deformation and transient and residual stresses during quenching in aluminum alloy W319 is presented. Rapid tension tests were performed on W319 in the supersaturated solution state at several temperatures and strain rates. A material model following the mechanical threshold stress (MTS)–Voce formulation is developed and implemented in both a simple one-dimensional code and a fully three-dimensional form as a user material subroutine in ABAQUS. The results of the tension tests are used to determine the parameters in the thermomechanical constitutive model. Unidirectional beam quenching experiments are performed to test the applicability of the constitutive model. Residual stresses in the beams are measured using a groove removal technique upon completion of the quenching process. Residual stress and deformation results from beam quenching experiments compare well to the analytical results computed using the constitutive model.

I. INTRODUCTION

IN recent years, there has been a continuous increase in the use of low-cost aluminum alloys to replace heavier or more expensive metals in automobile engine and suspension components. Cylinder heads, engine blocks, and other cast parts can be made both lighter and less expensive through the use of these alloys. Strength requirements are met by precipitation hardening, which involves a water quench, followed by an aging treatment at an intermediate temperature. The thermal gradients induced by the quench can lead to permanent, measurable part distortion and residual stresses.

Tight geometric tolerances for these applications requires that the distortion and residual stress be predicted consistently and accurately. The additional cost of machining a distorted part back into tolerance can easily offset the savings of using a low-cost alloy in the casting. Further, residual stresses can significantly decrease the fatigue life of such parts due to thermomechanical cycling. It is therefore important to predict and control quenching residual stresses.

We use a combination of rapid tension tests and beam quenching experiments similar to those of Aksel *et al.*[1,2] and Becker and co-workers[3,4] to develop a constitutive model for quenched, supersaturated W319. The constitutive model combines a creep model based on the work of Slavik and Sehitoglu[5] at high temperature with a phenomenological unified plasticity model based on the mechanical threshold stress (MTS) model of Follansbee and Kocks[6] for lower temperatures and higher strain rates.

M.L. NEWMAN, formerly with the Department of Mechanical and Industrial Engineering, University of Illinois Urbana–Champaign, Urbana, IL 61801, is with the Proctor and Gamble Company, West Chester, OH 45069. B.J. ROBINSON, formerly with the Department of Mechanical and Industrial Engineering, University of Illinois Urbana–Champaign, is with General Electric, Charleston, SC. H. SEHITOGLU and J.A. DANTZIG are with the Department of Mechanical and Industrial Engineering, University of Illinois Urbana–Champaign. Contact e-mail: dantzig@uiuc.edu

Manuscript submitted September 24, 2002.

The MTS model was developed for stage III hardening, and its use here, where stresses should be close to yield, should be considered as strictly phenomenological. The flow stress σ (MTS) is written as the sum of three components: an athermal stress σ_a, an "intrinsic strength" σ_i, which models yield, and a state variable σ_e, which evolves with deformation to model hardening. The terms σ_i and σ_e are further decomposed as a product of their respective values $\hat{\sigma}_i$ and $\hat{\sigma}_e$ in a reference state at 0 K and strain rate $\dot{\varepsilon}_0 = 10^7\ \mathrm{s}^{-1}$ with scaled temperature–strain rate parameters $S_i(\dot{\varepsilon}, T)$ and $S_e(\dot{\varepsilon}, T)$. In equation form, we have

$$\frac{\sigma}{\mu(T)} = \frac{\sigma_a}{\mu(T)} + S_i(\dot{\varepsilon}, T)\frac{\hat{\sigma}_i}{\mu_0} + S_e(\dot{\varepsilon}, T)\frac{\hat{\sigma}_e}{\mu_0} \qquad [1]$$

Here, $\mu(T)$ is the temperature-dependent shear modulus, given by Chen *et al.*,[7] as

$$\mu(T) = \mu_0 - \frac{3440}{\exp\left(\frac{215}{T}\right) - 1} \qquad [2]$$

where $\mu(T)$ is measured in Mega Pascals, T is measured in Kelvin, and $\mu_0 = 28.815$ GPa is the reference value at 0 K and $\dot{\varepsilon} = 10^7\ \mathrm{s}^{-1}$.

We use the velocity-modified temperature developed by MacGregor and Fisher[8] to scale the temperature and strain rate:

$$S_i(\dot{\varepsilon}, T) = \left[1 - \left[\frac{kT}{\mu(T)\mathbf{b}^3 g_{oi}} \ln\left(\frac{\dot{\varepsilon}_0}{\dot{\varepsilon}}\right)\right]^{\frac{1}{q_i}}\right]^{\frac{1}{P_i}} \qquad [3]$$

$$S_e(\dot{\varepsilon}, T) = \left[1 - \left[\frac{kT}{\mu(T)\mathbf{b}^3 g_{os}} \ln\left(\frac{\dot{\varepsilon}_0}{\dot{\varepsilon}}\right)\right]^{\frac{1}{q_e}}\right]^{\frac{1}{P_e}} \qquad [4]$$

Here, S_i and S_e are referred to as velocity-modified temperatures, and g_{oi} and g_{os} are the activation energy for flow at yield and saturation, respectively, normalized by Boltzmann's constant k, the Burgers vector $\mathbf{b}$, and the

shear modulus $\mu(T)$. The constant P_i, q_i, p_e, and q_e are related to the interaction of dislocation with precipitates in the matrix, but we simply treat them here as phenomenological constants. The values chosen are tabulated in Table I.

For large grain materials, such as cast W319, we assume that $\sigma_a = 0$, so that Eq. [1] becomes

$$\frac{\sigma}{\mu(T)} = S_i(\dot{\varepsilon}, T)\frac{\hat{\sigma}_i}{\mu_0} + S_e(\dot{\varepsilon}, T)\frac{\hat{\sigma}_\varepsilon}{\mu_0} \qquad [5]$$

At yield, $\hat{\sigma}_e = 0$, and the yield stress σ_y depends only on the intrinsic strength $\hat{\sigma}_i$, scaled by $S_i(\dot{\varepsilon}, T)$. Upon further loading, the flow stress is modeled through the evolution of $\hat{\sigma}_e$. Following Voce,[9,10] we posit a linear form

$$\frac{1}{\mu(T)}\frac{d\hat{\sigma}_e}{d\varepsilon} = \frac{\theta_0}{\mu_0}\left[1 - \frac{\hat{\sigma}_e}{\hat{\sigma}_{os}}\right] \qquad [6]$$

where θ_0 represents the slope of the stress-strain curve at yield in the reference state (0 K, $\dot{\varepsilon}_0 = 10^7\ s^{-1}$) and $\hat{\sigma}_{os}$ is a material parameter. In the work which follows, we set θ_0 to a constant value of 40 GPa. When $\hat{\sigma}_e = \hat{\sigma}_{os}$, the evolution rate of $\hat{\sigma}_e$ goes to zero, so $\hat{\sigma}_{os}$ is associated with saturation. Thus, the constitutive model parameters are $\{\hat{\sigma}_i, g_{oi}, \hat{\sigma}_{os}, g_{os}\}$. We describe in Section II how these parameters are determined from tensile tests.

The complete constitutive model includes a provision for creep deformation at high temperature and low strain rates. It is easier to understand how the transition from work hardening to creep is implemented after we show how the parameters in the MTS model are determined. We therefore reserve that discussion for the end of Section II.

II. DETERMINATION OF MODEL PARAMETERS

There are four parameters to be determined experimentally: $\hat{\sigma}_i$, g_{oi}, $\hat{\sigma}_{os}$, and g_{os}. The model is not very sensitive to the values of p_i, q_i, p_e, q_e, and θ_0, so we fix those to the values shown in Table I.

It is important to understand that heat treating distortion occurs in the first few seconds after quenching, while the material is still in supersaturated solid solution, and before any precipitation has occurred. We must determine the properties of the supersaturated solution at temperatures ranging from room temperature to the solution treatment temperature. Thus, conventional tensile testing is not appropriate, and we had to devise a method for testing the supersaturated solution before precipitation began. We now describe our approach, and give the results for a series of uniaxial tension tests performed to determine the constitutive parameters.

Table I. Constants in MTS–Voce Constitutive Model

Quantity	Symbol	Value	Units
Boltzmann's constant	k	1.38×10^{-23}	J/K
Burgers vector	$\mathbf{b}$	2.86×10^{-10}	m
Yield obstacle profile constant 1	p_i	0.5	—
Yield obstacle profile constant 2	q_i	1.5	—
Saturation obstacle profile constant 1	P_e	0.5	—
Saturation obstacle profile constant 2	q_e	2.0	—
Slope of $\sigma-\varepsilon$ at 0 K, $\dot{\varepsilon} = 10^7\ s^{-1}$	θ_0	40	GPa

Test bars 16 to 19 mm in diameter were sand cast in our laboratory after induction melting and degassing with flowing Ar gas. The dendrite arm spacing in the samples was measured at approximately 40 μm. Samples were then cut from the castings and machined to the final dimensions shown in Figure 1.

The specimens were then mounted in the grips of an Instron tensile testing machine, where they were heated *in situ* to the solution treatment temperature (495 °C). Three type K thermocouples were welded to the flat surface of the specimen to monitor temperature during the test. The specimen was held at the solution treatment temperature for a minimum of 4 hours, after which it was quenched rapidly using expanding nitrogen gas from a liquid nitrogen source. The thermocouples were monitored, so that when the specimen reached the desired testing temperature, it was pulled rapidly in uniaxial tension to determine the stress-strain response. In a typical test, the specimen was cooled from the solution treatment temperature to the test temperature in less than 5 seconds. An extensometer was used to record strain in the specimen during the test. Although care was taken to ensure that the temperature gradient across the specimen gage surface was as small as possible, temperature was difficult to control in this experiment, and it is estimated that there may have been variations of up to 20 °C across the gage surface.

Tests were conducted at a variet of strain rates and temperatures, resulting in the stress-strain curves shown in Figure 2. The modulus of elasticity was determined from the elastic portion of the stress-strain curves in these tests and fitted to a second-order polynomial:

$$E = 67{,}599 + 72.353T - 0.14767T^2 \qquad [7]$$

where E is in Mega Pascals and T is in Kelvin.[11]

To fit the constitutive equation parameters, we first extract the yield stress and saturation stress for each test. To do this, we differentiate the experimental stress-strain

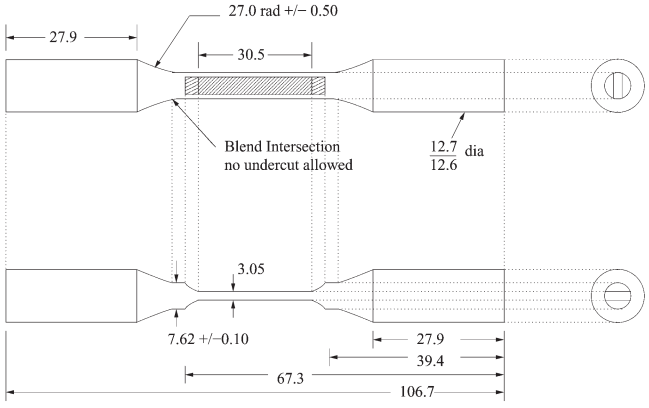

Fig. 1—Engineering drawing of tension-test specimen. Dimensions are given in millimeters.

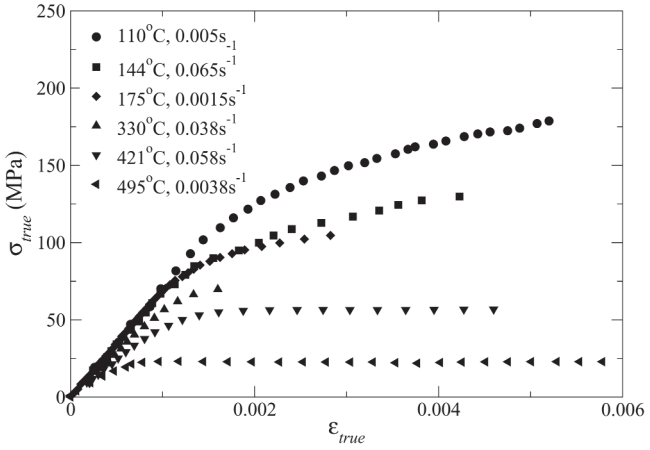

Fig. 2—Stress response of W319 specimens at different temperatures and strain rates.

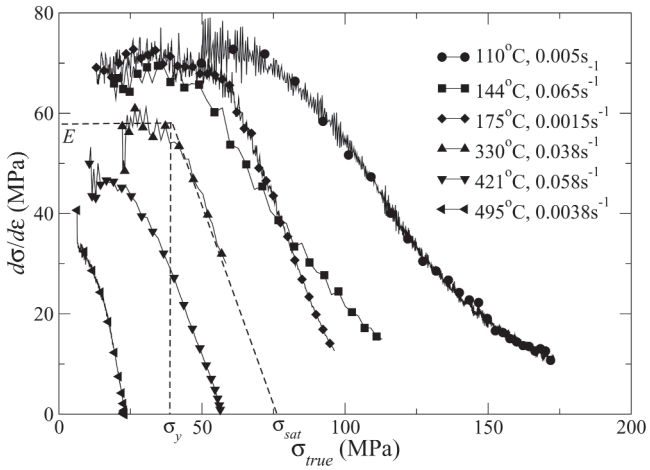

Fig. 3—Slope of stress-strain curve as a function of stress. Dashed lines are added to indicate how the elastic modulus, yield stress σ_y, and saturation stress σ_{sat} can be extracted from the data.

curve and plot the slope θ *vs* stress. We call these "θ plots." The stress-strain curves were somewhat noisy, and so we smoothed them by constructing a running average over 10 to 100 points before differentiation.

The results are shown in Figure 3, where we have also sketched in lines that can be used to interpret each curve. There should be an initial flat region, corresponding to the elastic portion of the stress-strain curve. After some stress level, θ decreases with stress corresponding to inelastic deformation. The Voce law (Eq. [6]) corresponds to a straight line for this portion of the curve, which seems to fit the data. The yield stress can be determined as the intersection of the initial flat region with the linear region. However, in many of our tests, especially at higher temperatures, the initial flat region was difficult to determine unequivocally. We chose instead to determine the yield stress using a 0.02 pct offset strain, and finding the intersection with the stress-strain curve. The saturation stress σ_{sat} is the intersection of the linear portion of the θ plot with the abscissa, *i.e.*, at $\theta = 0$. Note that even though the MTS–Voce model is simply a phenomenological choice, the data fit the parametric form reasonably well.

The intrinsic flow stress $\hat{\sigma}_i$ and the normalized activation energy g_{oi} can be determined from the yield data in uniaxial tension tests conducted at a known temperature and strain rate. At yield, $\sigma = \sigma_y$ and by definition $\hat{\sigma}_e = 0$. Substituting into Eqs. [3] and [5] and rearranging gives

$$\underbrace{\left(\frac{\sigma_y}{\mu(T)}\right)^{\frac{1}{2}}}_{Y} = \underbrace{\left(-\frac{1}{g_{oi}}\right)^{\frac{2}{3}}\left(\frac{\hat{\sigma}_i}{\mu_0}\right)^{\frac{1}{2}}}_{m} \underbrace{\left[\frac{kT}{\mu \mathbf{b}^3}\ln\left(\frac{\dot{\varepsilon}_0}{\dot{\varepsilon}}\right)\right]^{\frac{2}{3}}}_{x} + \underbrace{\left(\frac{\hat{\sigma}_i}{\mu_0}\right)^{\frac{1}{2}}}_{b} \quad [8]$$

Known quantities, and quantities that are measured in uniaxial tension tests, are grouped together in the *X* and *Y* terms of Eq. [8]. The two unknown parameters, g_{oi} and $\hat{\sigma}_i$, which appear in the *m* and *b* terms, are determined by plotting data from multiple uniaxial tension tests on an *X*-*Y* graph, called a Fisher plot, and fitting to a straight line. The result using our tensile test data is shown in Figure 4(a). The unknown parameters are then computed from the slope and intercept of the best-fit straight line.

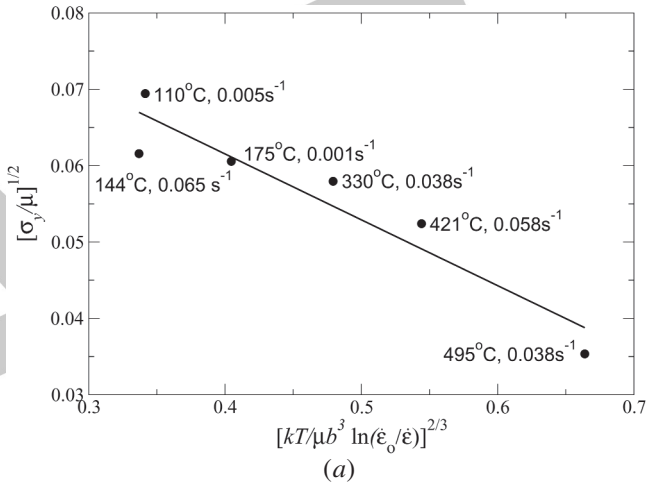

Fig. 4—(*a*) and (*b*) Fisher plots showing yield and saturation data from uniaxial tension tests of W319, with regression lines.

Using this method, we determined that $\hat{\sigma}_i = 265.7$ MPa and $g_{oi} = 1.18$.

The saturation stress data can be used in a similar way to determine values for the model parameters g_{os} and $\hat{\sigma}_{os}$. At saturation, the flow stress is σ_{sat}, and the state variable $\hat{\sigma}_e$ has evolved to its saturation value, $\hat{\sigma}_{os}$. The yield contribution has already been determined, so that we may substitute into Eqs. [4] and [5] and rearrange to find the following form:

$$\underbrace{\left(\frac{\sigma_{\text{sat}} - \sigma_y}{\mu(T)}\right)^{\frac{1}{2}}}_{Y} = \underbrace{\left(-\frac{1}{g_{os}}\right)^{\frac{1}{2}}\left(\frac{\hat{\sigma}_{\text{os}}}{\mu_0}\right)^{\frac{1}{2}}}_{m} \underbrace{\left[\frac{kT}{\mu \mathbf{b}^3}\ln\left(\frac{\dot{\varepsilon}_0}{\dot{\varepsilon}}\right)\right]^{\frac{1}{2}}}_{x} + \underbrace{\left(\frac{\hat{\sigma}_{\text{os}}}{\mu_0}\right)^{\frac{1}{2}}}_{b} \quad [9]$$

Thus, in a similar manner as in the determination of $\hat{\sigma}_i$ and g_{oi}, the experimental data are plotted in this form in Figure 4(b), along with the best fit straight line. From this graph, we extract the values $\hat{\sigma}_{os} = 341.1$ MPa and $g_{os} = 0.562$.

Figure 5 shows the stress-strain curves predicted by using these model parameters to simulate uniaxial tension tests under the same conditions as the experiments. The response is well predicted by the model, except for the two tests at 110 °C and 144 °C. It is not possible for the MTS–Voce model to fit both of these tests well, since the Fisher parameters for the two tests are very similar, but saturation occurs at significantly different values. The discrepancy is attributed to errors in temperature measurement in the experiments.

The constitutive model also includes a provision for modeling creep deformation at high temperature and low strain rate. A model for the creep behavior of W319 has been developed by Sehitoglu and co-workers.[5,12] They relate flow stress σ to the creep strain rate $\dot{\varepsilon}$ *via*

$$\sigma = 1 \times 10^{-3} K(T)\dot{\varepsilon}^{0.33} \quad [10]$$

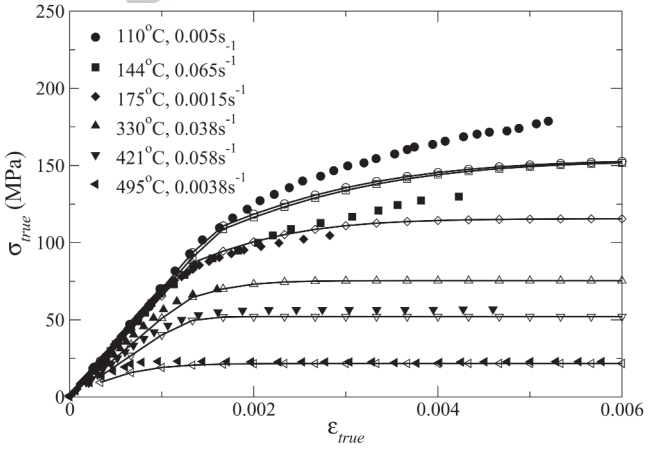

Fig. 5—Comparison of true stress *vs* true strain in uniaxial tension. Experimental data are shown with filled symbols, and the corresponding conditions from the model are shown with empty symbols.

where $\dot{\varepsilon}$ is measured in s^{-1} and the drag stress $K(T)$, measured in MPa, is given by

$$K(T) = 52.4797 + 0.0561T - 1.146 \times 10^{-4} T^2 \quad [11]$$

and T is measured in Kelvin. Note that the power law form given in Eq. [10] is consistent with the solute drag mechanism proposed by Cottrell and Jaswon.[13]

At high temperatures and low strain rates, creep will be the dominant deformation mechanism, whereas work hardening will be the dominant deformation mechanism at lower temperatures and higher strain rates. In order to model the transition between the two deformation mechanisms, we assume that the mechanism with the lower flow stress will be selected. For any given strain rate and temperature, the flow stress from the MTS–Voce model can be computed from Eq. [5], and the flow stress for creep can be computed from Eq. [10]. For each temperature, there is a transition strain rate $\dot{\varepsilon}_{tr}$ below which Eq. [10] predicts a lower flow stress. We computed $\dot{\varepsilon}_{tr}$ for a number of temperatures, and fitted the following equation for the transition strain rate:

$$\dot{\varepsilon}_{tr} = \exp\left[-38.859 + 0.104T - 6.3247 \times 10^{-5} T^2\right] \quad [12]$$

where $\dot{\varepsilon}_{tr}$ is in s^{-1} and T is in Kelvin.

We found that making an abrupt transition from one deformation mechanism to the other during computation led to occasional difficulties in convergence. We therefore enforced a smooth transition between the two by using the parameter β defined by

$$\beta = \frac{1}{2}\left[1 + \tanh\left(\frac{\dot{\varepsilon} - \dot{\varepsilon}_{tr}}{2\dot{\varepsilon}_{tr}}\right)\right] \quad [13]$$

After evaluating the plastic flow stress σ^p using Eq. [5], and the creep stress σ^c using Eq. [10], the flow stress used in the model is computed as

$$\sigma = \beta\sigma^p + (1 - \beta)\sigma^c \quad [14]$$

This provides a smooth transition between the two deformation modes, aiding convergence.

III. BEAM-QUENCHING EXPERIMENTS

The objective of this study was to develop a predictive tool for the quenching response of W319. To that end, we conducted beam-quenching experiments similar to those first described by Aksel *et al.*[1,2] and further developed by Becker and co-workers.[3,4] The beams were quenched on one side, leading to thermal gradients, which caused inelastic bending deformation.

The beams for the quenching experiments were sand cast in our laboratory using the same methods described earlier for the tensile specimens. They also had similar microstructure, with dendrite arm spacing of approximately 40 μm. The beams were cast slightly oversized, and then milled to their final dimensions. In the basic experiment, a beam measuring 306 × 20 × 60 mm was quenched from the solution treatment temperature (495 °C). The beam was supported on knife edges 280 mm apart, and rested approximately 4 mm deep in agitated water at 25 °C, as shown in Figure 6. One of the knife edges was

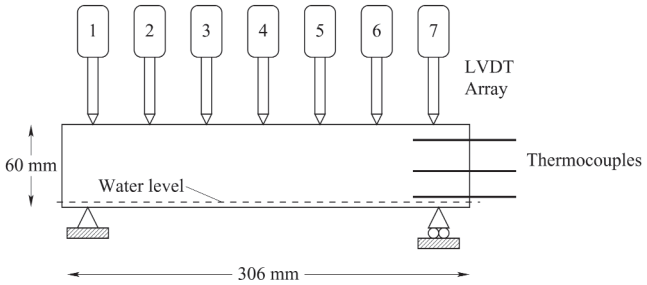

Fig. 6—Schematic of beam-quenching apparatus.

fixed, while the other was mounted on a roller to allow the beam to expand laterally without constraint. The depth of the specimen in the quenchant was controlled by a float-switch-activated cutoff valve between an auxiliary water tank and the quenchant tank.

Transient displacement of the top surface (opposite the quenchant) was measured using seven linear variable displacement transducers (LVDTs) spaced 46.7 mm apart, such that the end transducers were directly above the supports and all transducers were evenly spaced with respect to one another. All of the LVDTs had sharp-pointed contact tips to ensure that there was no transverse slippage of the contact point on the beam's top surface. The LVDTs had a vertical range of motion of ±3 mm and a resolution of 10 μm.

Temperatures in the beam were recorded at three distances from the quenched surface using type-K thermocouples with a 0.5-mm bead, cemented into 1-mm-wide holes drilled 20 mm deep into the beam end (Figure 6). The beams were heated in a bench-top convection furnace at 495 °C to 505 °C for at least 4 hours. Insulation panels rested on the sides of the beam in the furnace while heating. The beam was then moved rapidly from the furnace with the insulation attached to minimize heat losses due to convection with ambient air to the supports in the quenchant tank, where the water level was held at approximately 5 mm below the bottom surface of the beam. Once the beam was in place, the LVDTs were positioned on the top surface of the beam, and the insulation panels on the sides of the beam were moved to a distance of 5 mm from the sides of the beam, to prevent water from wicking between the beam and insulation. The elapsed time for this procedure, from the opening of the furnace to the placement of the LVDTs, was approximately 30 seconds.

Water at ambient temperature was then introduced into the quench tank from an auxiliary water tank. During this process, the water was agitated by means of two magnetic stirring bars propelled by motors underneath the quenchant tank. When the water level reached a point 4 mm above the bottom surface of the beam, a float switch halted passage of water from the auxiliary tank. Displacement of the top surface of the beam and temperatures in the interior were recorded at 200 Hz from the LVDTs and thermocouples, using a National Instruments data acquisition system controlled by Lab View 4.0.

Typical temperatures recorded by the thermocouples in the quenched beam and the water bath are shown in Figure 7. Note that the entire beam is close to a uniform temperature within about 5 minutes after the start of the

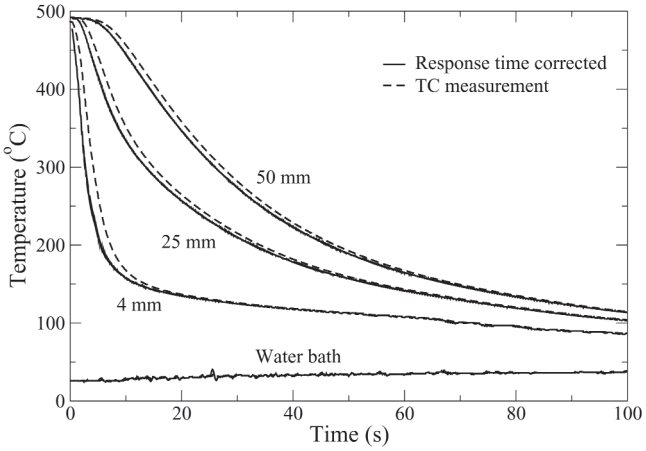

Fig. 7—Temperature history of the quenched beam measured at three interior locations, along with values corrected for thermocouple lag.

quench, and that the quenchant temperature increases by no more than 20 °C over the course of the experiment.

Also shown in the figure are temperatures corrected for the temporal lag of the thermocouples. The size, thermal mass, and thermal contact resistance of the thermocouple prevent it from responding instantaneously. A method developed by Dantzig[14] was used to reconstruct the more accurate temperature history from the thermocouple data. The thermocouple output was measured as it was inserted into a hole in a piece of W319 at the solution treatment temperature. Once the thermocouple had reached the bottom of the hole, an exponential rise in temperature was observed. This is a variation of the so-called plunge test, which is used to measure the response time τ of a thermocouple. The thermocouple response was fitted to the following form:[14]

$$\frac{T' - T_{Al}}{T_i - T_{Al}} = \exp\left\{-\frac{t}{\tau}\right\} \qquad [15]$$

where T' is the temperature recorded by the thermocouple, T_i is the initial thermocouple temperature, and T_{Al} is the temperature of the aluminum. The best fit to the experimental data gave a response time determined of 1.3 seconds.[11]

Once the thermocouple response function is known, a more accurate temperature history $T(t)$ can be reconstructed from the measured thermocouple response $T'(t)$ using[14]

$$T(t) = T'(t) + \tau \frac{dT'(t)}{dt} \qquad [16]$$

We used this equation to reconstruct the temperature history from the measured data.

In order to use the model most effectively, we also wanted to simulate the thermal response of the beam in the water quench. We characterized the quench through a heat-transfer coefficient $h(T)$, which was a function of the interface temperature. We simulated the thermal response of the beam using FIDAP*, with a user subroutine to represent

*FIDAP is a trademark of . . .

$h(T)$. An objective function G was defined as the total error between experimental and computed temperatures at equivalent locations:

$$G = \sum_{k=1}^{N} \sqrt{\sum_{j=1}^{3} (\bar{T}_j - T_j)^2} \qquad [17]$$

where N is the number of discrete targets in the critical quench section (typically, 10 to 12), $\bar{T}_j$ is the experimental temperature, and T_j is the predicted temperature. We represented $h(T)$ using a fifth order polynomial, and used DOT** optimization software to find the polynomial

**DOT is a trademark of . . .

coefficients which minimized G.[15] The optimized HTC was given by

$$log\,[h(\hat{T})] = 32.358\hat{T}^5 - 133.25\hat{T}^4 + 187.05\hat{T}^3 - 110.46\hat{T}^2 + 23.384\hat{T} - 2.6226 \qquad [18]$$

where $h(\hat{T})$ is measured in W/mm^2 K, and the temperature T in Kelvin has been scaled to ensure that the polynomial coefficients are of similar order as

$$\hat{T} = \frac{T - 366}{1000 - 366} \qquad [19]$$

This heat-transfer coefficient was then used in thermal finite-element analyses to determine the complete temperature history in the quenched beams. Because there are no outside forces acting on the beam (due to the simple supports), this temperature history, combined with the known thermal expansion coefficient, provides the complete input to the structural problem.

The vertical deflection of the beam recorded by the seven LVDTs during quenching was very reproducible from bar to bar. A typical result is shown in Figure 8, where the displacement transducers are numbered from left to right. If the beam deformation is symmetric about the horizontal midplane, the deflections recorded by the LVDT pairs (1, 7), (2, 6), and (3, 5) should match, as can be seen in Figure 8.

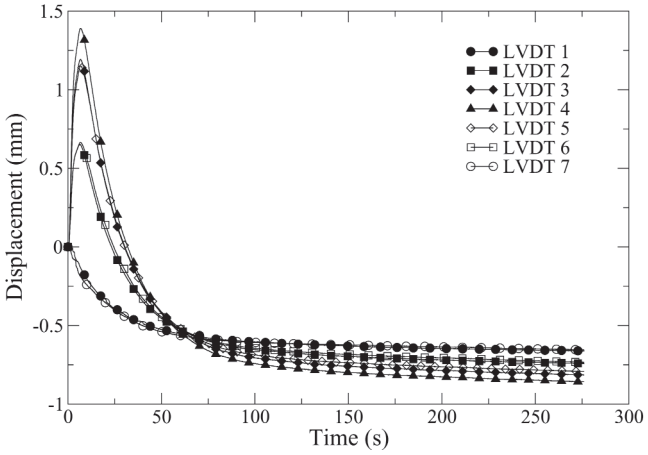

Fig. 8—Deflection of the top surface of the quenched beam, recorded at 46.67-mm intervals along the top surface.

For this simple geometry, the beam should deflect in an arc of constant curvature.[1] Accordingly, we use deflection data from adjacent LVDTs to compute κ the curvature of the beam:

$$\kappa = 2\left(\frac{\delta z_2 - \delta z_1}{dx_2^2 - dx_1^2}\right) \qquad [20]$$

where δz_i is the deflection measured by LVDT i, and δx_i, is the distance of transducer i from the center of the beam. If the beam bends in a circular arc, then the curvature computed for each pair of adjacent transducers should be the same. Figure 9 shows the curvatures derived from the transducer pairs listed previously.

The curvatures obtained using the LVDT 4 (located at the center of the beam) are not in good agreement with either each other or the remainder of the curvatures. This was typical of all experiments. Also notable is the larger amount of noise in these curvatures. These two observations, along with an analysis of the deflection data used in the curvature equation, suggest that the experimental uncertainty in measurement of the deflection between the center and adjacent LVDTs is on the order of the difference between these two measurements. For this reason, curvatures measured using the center LVDT are discarded in the results that follow, and an average curvature of the beam is computed using the remaining four curvatures computed using the outer six LVDTs.

Following Aksel *et al.*,[1,2] we analyze the deformation as one-dimensional plane stress. Temperature is assumed to vary only in the direction perpendicular to the quenched face, *i.e.*, $T = T(z)$, and the only nonzero stress is $\sigma_{xx}(z)$. The strain compatibility relations for this case reduce to[16,17]

$$\frac{\partial^2 \varepsilon_{xx}}{\partial z^2} = 0 \qquad [21]$$

Integrating this expression twice, and decomposing the total strain into a sum of the elastic strain σ_{xx}/E, thermal strain $\alpha T(z)$ and inelastic strain ε_{xx}^{in} yields

$$\sigma_{xx}(T) = E(C_1 z + C_2 - \alpha T(z) - \varepsilon_{xx}^{in}(z) \qquad [22]$$

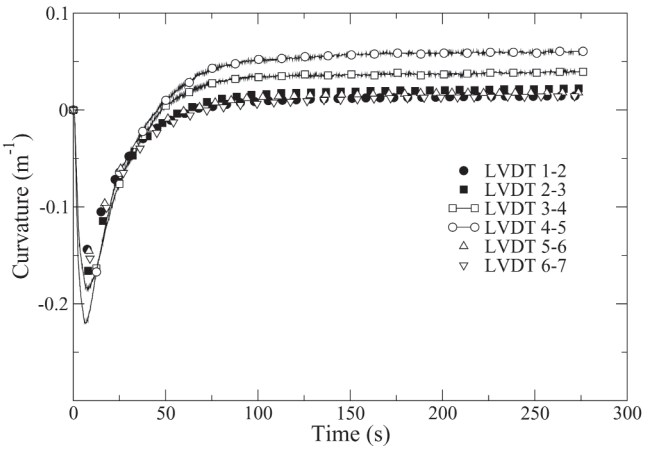

Fig. 9—Curvature of beam determined from adjacent LVDT pairs, with curvatures obtained using center LVDT shown with a line to emphasize the noise in these measurements.

The constants of integration C_1 and C_2 are evaluated by enforcing force and moment equilibrium across the beam $-h \le z \le h$:

$$\int_{-h}^{h} \sigma_{xx}(z)dz = 0; \qquad \int_{-h}^{h} \sigma_{xx}(z)zdz = 0 \qquad [23]$$

After evaluating C_1 and C_2, we may then substitute the results into Eq. [22] and rearrange to write the total strain as

$$\varepsilon_{xx}(z) = \frac{3z}{2h^3}\int_{-h}^{h} \alpha T\, zdz + \frac{3z}{2h^3}\int_{-h}^{h} \varepsilon_{xx}^{in}\, zdz + \frac{1}{2h}\int_{-h}^{h} \alpha T dz + \frac{1}{2h}\int_{-h}^{h} \varepsilon_{xx}^{in}\, dz \qquad [24]$$

We actually use this equation in the incremental form

$$\Delta\varepsilon_{xx}(z) = \frac{3z}{2h^3}\int_{-h}^{h} \alpha \Delta T z dz + \frac{3z}{2h^3}\int_{-h}^{h} \Delta\varepsilon_{xx}^{in}\, zdz + \frac{1}{2h}\int_{-h}^{h} \alpha \Delta T dz + \frac{1}{2h}\int_{-h}^{h} \Delta\varepsilon_{xx}^{in}\, dz \qquad [25]$$

The complete temperature history of the beam at all locations was provided from a thermal finite-element model. We begin the analysis with an undeformed beam at the uniform solution treatment temperature, and then step through time, applying the precomputed thermal loads incrementally. The beam is discretized spatially, typically into 300 equal intervals, and Eq. [25] is integrated at each point. The integration must be performed iteratively, because $\Delta\varepsilon_{xx}^{in}$ depends on the temperature, strain rate, and state variable $\hat{\sigma}_e$. The solution is obtained through the following procedure, where k indicates the iteration counter:

(1) Given ΔT (z), guess $(\Delta\varepsilon_{xx}^{in})^{(k+1)} = (\Delta\varepsilon_{xx}^{in})^{(k)}$.
(2) Solve Eq. [25] for $(\Delta\varepsilon_{xx})^{(k+1)}$ and σ_{xx}, which satisfy force and moment equilibrium in beam.
(3) Use the MTS–Voce constitutive model from Eq. [5] to find $(\Delta\varepsilon_{xx}^{in})^{(k+1)}$. Note that these depend on the local value of the set (T, $\dot{\varepsilon}$, $\hat{\sigma}_e$).
(4) Use $(\Delta\varepsilon_{xx}^{in})^{(k+1)}$ from step 3 to determine $(\Delta\varepsilon_{xx})^{(k+1)}$ in Eq. [25]

Steps 2 through 4 are repeated until a self-consistent pair $\Delta\varepsilon_{xx}^{in}$ and $\Delta\varepsilon_{xx}$ are determined. The state variable $\hat{\sigma}_e$ is then updated for this location. This procedure is repeated at all spatial increments, and then the time is incremented until the entire temperature history has been completed.

Figure 10 shows predictions of the constitutive model determined using this procedure, compared with the experimental data. The agreement between the experiments and the model is reasonably good, but the residual distortion is underpredicted. The curvature deviation is small in comparison to previous work with different alloys and constitutive models by Aksel *et al.*[2] and Karabin *et al.*[4]

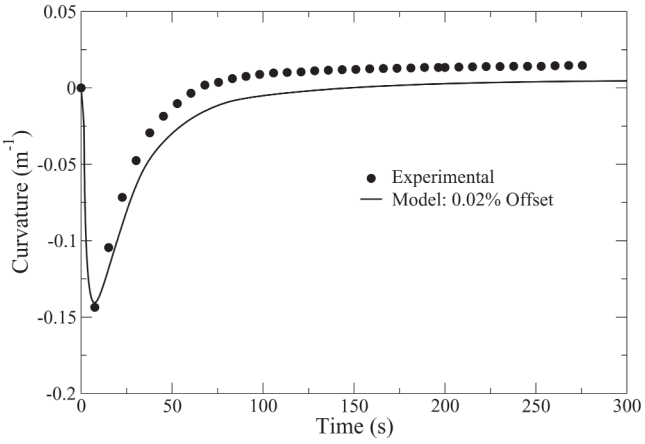

Fig. 10—Transient curvature in a quenched beam predicted by unified model using tensile test data parameters, compared to measurements.

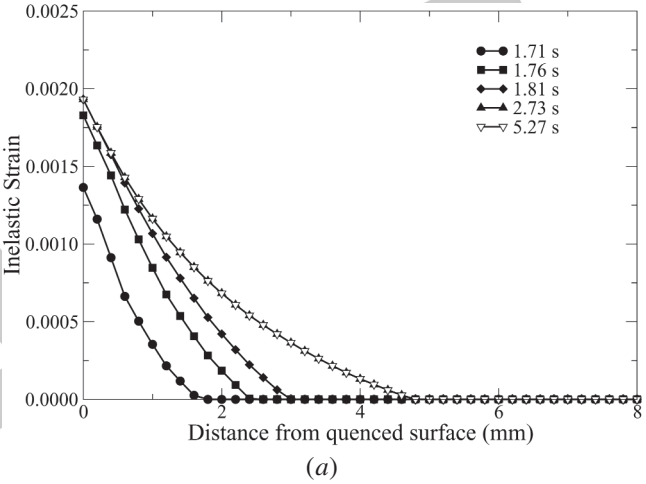

(*a*)

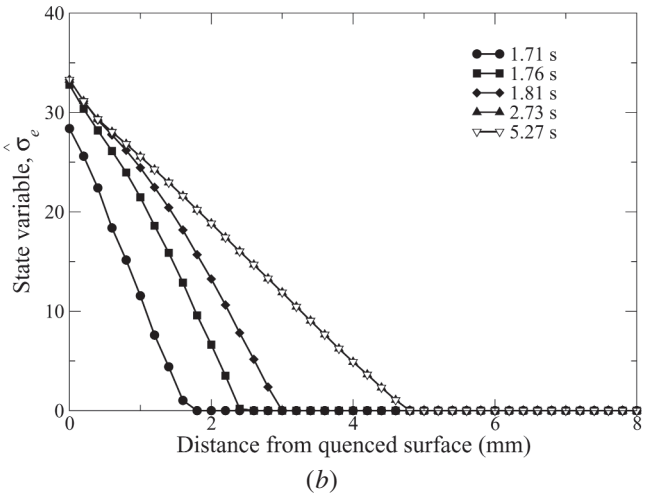

(*b*)

Fig. 11—(*a*) and (*b*) Development of inelastic deformation in the beam for small quenching times. Note that there is no more inelastic deformation after 2.73 s, and that the inelastic deformation is confined to the 5 mm of material closed to the quenched end.

Figure 11 depicts the evolution of the plastic strain and the state variable for some early times. Tensile plastic strain develops in the region within 5 mm of the quenched

surface and the state variable evolves concomitantly. The stress scaled by MTS yield stress is displayed in Figure 12. At 2.73 seconds, stress relaxation becomes evident within several millimeters of the quenched surface as thermal gradients have decreased from their peak values.

IV. RESIDUAL STRESS MEASUREMENTS

Another important quantity for quenching applications is the residual stress in the part. This is relatively difficult to measure, making an accurate constitutive model very valuable for manufacturing applications. Residual stress in the quenched beams was measured using a groove-removal technique in which a wide groove of material was extracted by clamping one end of the beam and then milling from the center in 0.127 ± 0.01-mm thin strips, as illustrated in Figure 13. A strain gage opposite the removed groove recorded deformation during the free-bending relaxation of the beam. Two minutes elapsed after each mill pass before reading the strain gage, to allow the beam temperature to equilibrate. Grooves were cut starting from the quenched surface or the dry (top) surface on several beams to construct a full representation of the residual stress. Using multiple beams is validated by the reproducibility of the curvatures in different experiments, and also by the fact that the residual stress measurements agree at the center when starting from opposite sides of the beam. A finite-element analysis showed that predicted strain using the groove-removal technique is nearly identical to that predicted by removing an entire layer of material. Groove removal is the preferable of the two techniques since the clamping mechanism need not be disengaged after the removal of each layer. Therefore, strain can be assessed at more frequent intervals.

The residual stress state was inferred from the strain gage measurements using an inverse technique developed by Leeser and Danne,[18] which assumes elastic deformation during relaxation. Strain compatibility and force and moment equilibrium are used to give the residual stress as a function of the remaining beam thickness w:

$$\sigma(w) = E\left[2\varepsilon_G + \frac{1}{2}w\frac{d\varepsilon_G}{dw} - 3w\int_w^{2h}\frac{\varepsilon_G}{w^2}dw\right] \quad [26]$$

where ε_G is the strain measured by the strain gage and h is the beam half-height. The measured residual stress is compared to the stress predicted using the unified plasticity-creep model in Figure 14. The agreement is very good. Karabin *et al.*[4] has pointed out that residual stress is less dependent on the constitutive model than distortion. However, our model predicts both very well.

V. DISCUSSION

The combination of experiments and constitutive model described in the previous sections works well for predicting the distortion and residual stress in quenched W319. Although the MTS–Voce constitutive model was developed for stage III hardening, we have used it as a phenomenological framework for the constitutive behavior.

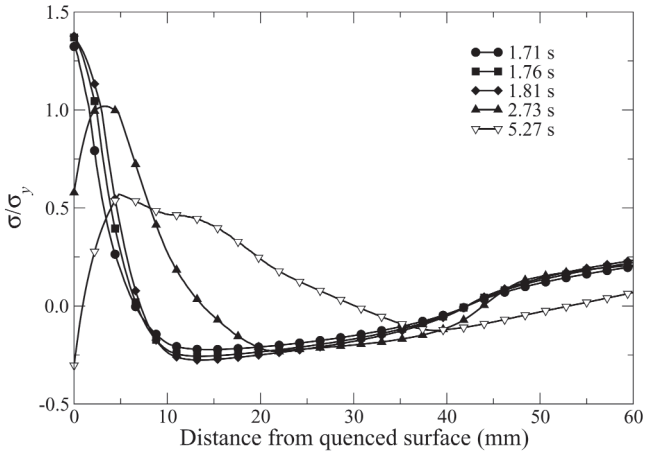

Fig. 12—Stress divided by local yield stress for early times after quenching. Note that the stress state changes after 2.73 s, even though the inelastic strain does not, because the temperature change leads to a change in yield stress.

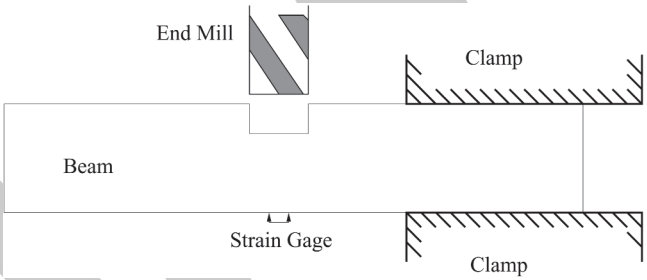

Fig. 13—Sketch of fixturing apparatus used in groove-removal technique.

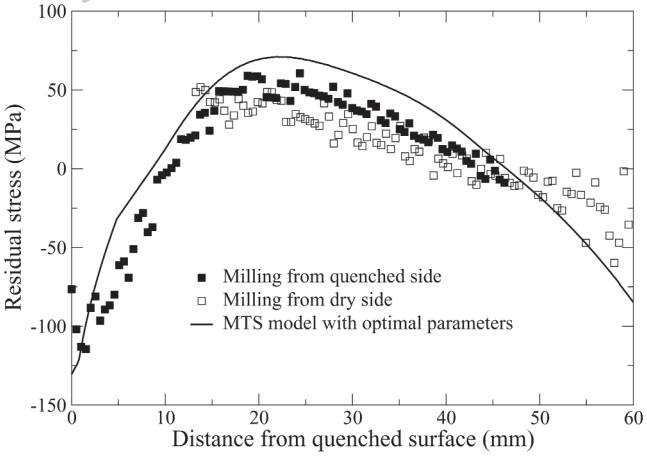

Fig. 14—Residual stress predictions of MTS–Voce and unified constitutive models, compared to experimental measurements.

We did try other models, such as the popular hyperbolic sine model, but found that they did not have enough parameters to fit all of the data over the wide range of temperatures and strain rates that we consider here. The MTS–Voce model has parameters that allow matching both yield and saturation, and thus allow us to model the entire inelastic region. The MacGregor–Fisher velocity-modified temperatures given in Eqs. [3] and [4] allow us to do so over a wide range of temperatures.

The uniaxial tensile tests, which provided the basis for determining the material parameters, were difficult. Nevertheless, it is remarkable that the parameters extracted from these tests performed well in the prediction of behavior during quenching. It should be noted that most of the inelastic deformation in our experiments occurs near yield. Thus, the amount of inelastic deformation in the quenching simulations is most sensitive to the parameters that determine the yield points, g_{oi} and $\hat{\sigma}_i$. Because they determine the material response after yield, the model is also sensitive to the parameters g_{os} and $\hat{\sigma}_s$. The model is relatively insensitive to the obstacle profile constants p_i, q_i, p_e, q_e and θ_0.

It is important to realize that the data we have given apply only to quenching of the supersaturated solid solution. The microstructure is essentially constant in our tensile tests and beams over the time of the experiments. If one were to model slower cooling rates, where precipitation would be expected to occur, we would expect the model not to perform nearly as well. Cloutier *et al.*[19] described an approach to such a model, based on the work of Shercliff and Ashby,[20] where a state variable is used to track the evolution of the microstructure. In our model, this could be accommodated through the introduction of a state variable into the expressions for $\hat{\sigma}_i$ and $\hat{\sigma}_e$. Collecting data for such a model would be challenging, especially at elevated temperatures, where it would be difficult to find a stable microstructure to test.

VI. CONCLUSIONS

We have studied the response of W319 during quenching. A constitutive model based on the MTS–Voce formulation of Follansbee and Kocks[6] has been used to describe the mechanical behavior. Rapid tensile testing was performed at a variety of temperatures and strain rates to provide data to determine the model parameters. One-dimensional quenching experiments were performed on simple cast W319 beams. Deformation results from these tests were characterized as curvature. Deformation measured in these experiments compared well with computational results.

ACKNOWLEDGMENTS

This work was supported under a grant from the Ford Foundation, under the University Research Program. The experiments that led to the development of the constitutive models were carried out at the University of Illinois by Dr. X.Y. Zhang. The authors also thank A. Beaudoin, University of Illinois, and J. Allison and J. Zindel, Ford Scientific Research Lab, for helpful discussions and guidance.

REFERENCES

1. B. Aksel: Ph.D. Thesis, Cornell University, 1990.
2. B. Aksel, W. Arthur, and S. Mukherjee: *J. Eng. Industry*, 1992, vol. 114, pp. 309-16.
3. R. Becker, M. Karabin, J. Liu, and R. Smelser: *Trans. ASME: J. Appl. Mech.*, 1996, vol. 63, pp. 699-705.
4. M. Karabin, R. Becker, and P. Vranka: *The Integration of Material, Process and Product Design*, 1999, pp. 129-37.
5. D. Slavik and H. Sehitoglu: *Thermal Stress, Material Deformation, and Thermo-Mechanical Fatigue*, ASME PVP, 1987, vol. 123, pp. 65-74.
6. P. Follansbee and U. Kocks: *Metall. Trans. A*, 1988, vol. 19A, pp. 81-93.
7. S. Chen, M. Stout, U. Kocks, S. MacEwen, and A. Beaudoin: in *Hot Deformation of Aluminum Alloys II*, T.R. Bieler, L.A. Lalli, and S.R. MacEwen, eds., 1998, pp. 205-16.
8. C. MacGregor and J. Fisher: *Trans. ASME: J. Appl. Mech.*, 1946, vol. 13 (1), pp. 11-16.
9. E. Voce: *J. Inst. Met.*, 1948, vol. 74, pp. 537-62.
10. E. Voce: *Metallurgica*, 1955, vol. 51, pp. 219-25.
11. M. Newman: Ph.D. Thesis, University of Illinois, Urbana–Champaign, Urbana, IL, 2001.
12. T.J. Smith, H.J. Maier, H. Sehitoglu, E. Fleury, and J.A. Allison: *Metal. Matter. Trans. A*, 1999, vol. 30A, pp. 133-46.
13. A.H. Cottrell and M.A. Jaswon: *Proc. R. Soc. A*, 1949, vol. 199, pp. 104-14.
14. J. Dantzig: *Rev. Scientific Instrum.*, 1985, vol. 56 (5), pp. 723-25.
15. G. Vanderplaats: *Numerical Optimization Techniques for Engineering Design: With Applications*, McGraw-Hill Book Company, New York, NY, 1984.
16. A. Mendelson: *Plasticity: Theory and Application*, Robert E. Krieger Publishing Company, 1968.
17. B. Boley and J. Weiner: *Theory of Thermal Stresses*, Dover Publications, Inc., 1960.
18. D. Leeser and R. Danne: *Proc. Society for Experimental Stress Analysis*, 1954, vol. 12 (1), pp. 203-08.
19. C. Cloutier, P. Reeber-Schmanski, J. Jones, and J. Allison: in *Automotive Alloys 1999*, S. Das, ed., 1999, pp. 153-160.
20. H. Shercliff and M. Ashby: *Acta Metall. Mater.*, 1990, vol. 38 (10), pp. 1789-1802.

Annotations from 02482A4.pdf

Page 1

Annotation 1; Label: IPC; Date: 4/25/2003 9:39:34 AM
Former and current titles of positions for all authors? Zip code for Charleston?

Annotation 2; Label: IPC; Date: 4/25/2003 9:39:46 AM
Is "Mega Pascals" okay?

Page 2

Annotation 1; Label: IPC; Date: 4/25/2003 9:40:01 AM
Vendor name and location?

Annotation 2; Label: IPC; Date: 4/25/2003 9:40:12 AM
Is "Mega Pascals" okay?

Page 5

Annotation 1; Label: IPC; Date: 4/25/2003 9:40:41 AM
Location of National Instruments?

Annotation 2; Label: IPC; Date: 4/25/2003 9:40:50 AM
Vendor name and location?

Annotation 3; Label: IPC; Date: 4/25/2003 9:41:06 AM
Trademark holder and location?

Page 6

Annotation 1; Label: IPC; Date: 4/25/2003 9:41:23 AM
Trademark holder and location?

Page 9

Annotation 1; Label: IPC; Date: 4/25/2003 9:41:44 AM
Reference 1: Location of publisher?

Annotation 2; Label: IPC; Date: 4/25/2003 9:42:00 AM
Reference 5: Location of publisher?

Annotation 3; Label: IPC; Date: 4/25/2003 9:42:10 AM
Reference 17: Location of publisher?

Annotation 4; Label: IPC; Date: 4/25/2003 9:42:27 AM
Reference 4: Publisher and location?

Annotation 5; Label: IPC; Date: 4/25/2003 9:42:39 AM
Reference 7: Publisher and location?

Annotation 6; Label: IPC; Date: 4/25/2003 9:42:51 AM
Reference 18: Publisher and location?

Annotation 7; Label: IPC; Date: 4/25/2003 9:42:56 AM
Reference 19: Publisher and location?

Online Proofing Guidance Page

FIRST STEP:

Install Adobe Acrobat Reader if you do not already have this or another Acrobat product installed on your computer. You can do this free of charge by connecting to the Adobe site and following the instructions at:

http://www.adobe.com/products/acrobat/readermain.html

SECOND STEP:

Please download and print your PDF file — we recommend that you save this file to disk, rather than opening it from within your Browser.

From a PC:

1. Right-click on the file/article link.
2. Select ''Save Target as''
3. Select a desired location on your computer to save the file to, and click on ''Save''
4. Open your PDf file directly with Acrobat Reader or another Acrobat product.
5. Print this file as you normally would with any typical application. Example: Go up to your toolbar, select ''File'', select ''Print''.

From a MAC:

1. Hold the mouse button down over the link.
   a. In Internet Explorer, select ''Download Link to Disk'' from the resulting pop-up menu
   b. In Netscape, select ''Save this Link as'' from the resulting pop-up menu
2. Select a desired location on your computer and click on ''Save''
3. Open your PDF file directly with Acrobat Reader or another Acrobat product.
4. Print this file as you normally would with any typical application. Example: Go up to your menu bar, select ''File'', select ''Print''.

THIRD STEP:

Please go through the file you have just printed and thoroughly and clearly mark any revisions you would like to see implemented in your paper. If you have had any changes in phone/fax or e-mail addresses since your paper was submitted, please send us this new information.

FOURTH STEP:

Your revised paper needs to be faxed or mailed to:

IPC Communication Services
Attn: Sheryl Dickenson
501 Colonial Drive
St. Joseph, MI 49085
Fax number: 1-269-983-4064

If you have questions regarding your paper in general, you may email or telephone:

IPC Communication Services
Attn: Sheryl Dickenson
Email: sdickens@ipcjci.com
Phone: 1-269-983-7412, ext. 529